



# High Rate Deposition in Cold Spray

Ozan C. Ozdemir<sup>1</sup> · Patricia Schwartz<sup>1</sup> · Sinan Muftu<sup>1</sup> · Forest C. Thompson<sup>2</sup> · Grant A. Crawford<sup>2</sup> · Aaron T. Nardi<sup>3</sup> · Victor K. Champagne Jr.<sup>3</sup> · Christian A. Widener<sup>4</sup>

Submitted: 6 April 2020 / in revised form: 2 October 2020 / Accepted: 20 November 2020 / Published online: 3 January 2021  
© ASM International 2021

**Abstract** Industrialization of cold spray introduces concerns regarding the cost and time efficiency of cold spray procedures. In this work, high rate deposition of tantalum was studied computationally and experimentally. Quasi-1D multiphase fluid simulations predicted minimal effects on the bonding conditions of particles with 5% to 14% increase in powder-to-gas mass flow ratio. Experimental specimens were produced to observe the mechanical and microstructural effects of increased powder stream loading. Adhesion and hardness tests as well as thermal conductivity, optical microscopy, and electron backscatter diffraction examinations only exhibited minor differences in the mechanical and microstructural properties of the specimens. The increased powder stream loading rate, however, allows a significant reduction in the time required for depositing the same amount of tantalum by a factor of three. The results of the study enable shorter cold spray deposition time. This leads to significant cost savings associated with consumption of helium and labor, while

facilitating shorter turn-around times for repairing components and manufacturing of cold-sprayed products.

**Keywords** cold spray · tantalum · helium · high rate deposition · optimization

## Introduction

As cold spray (CS) applications are industrialized, conservation of process resources and cost effectiveness improvements become increasingly important. By reducing spray duration for parts, coatings, and repairs, productivity can be significantly increased and thus CS can be made even more attractive to a broad range of industries. In the case of cold spraying with helium, the gas costs are very high as helium is a nonrenewable resource that escapes into space after being released into the atmosphere (Ref 1, 2). Process cost reduction is closely tied to the mass flow ratio of the powder to the amount of process gas flowing through the nozzle, also known as the *particle loading rate*. Measured in percentage, particle loading rate is a non-dimensional parameter that provides a measure of how effectively the gas consumption is being utilized. While recovery systems may help reduce gas costs significantly in cold spray facilities that consume significant amounts of helium, optimization of powder feeding rates can further reduce helium demand per component while simultaneously decreasing labor costs and increasing production rates. Optimization of particle loading rate can also benefit a given process that employs nitrogen or air as the propellant gas by maximizing the material deposition rate to reduce manufacturing time and associated costs. These positive economic benefits of increasing particle loading rate by means of increasing powder feed rate or reducing

Production Notes: ITSC credit line: This article is an invited paper selected from presentations at the 2019 International Thermal Spray Conference, held May 26–29, 2019 in Yokohama, Japan and has been expanded from the original presentation.

✉ Ozan C. Ozdemir  
o.ozdemir@northeastern.edu

- <sup>1</sup> Department of Mechanical and Industrial Engineering, Northeastern University, Boston, MA, USA
- <sup>2</sup> Arbogast Materials Processing & Joining Laboratory, South Dakota School of Mines & Technology, Rapid City, SD, USA
- <sup>3</sup> Army Research Laboratory, Aberdeen Proving Ground, Aberdeen, MD, USA
- <sup>4</sup> VRC Metal Systems, Rapid City, SD, USA

nozzle throat size in a given cold spray process have been previously discussed by Ozdemir et al. (Ref 3), Stier (Ref 4), and Gabel (Ref 5).

While the economic benefits are recognized, the effects and limitations of increasing the particle loading rate need to be carefully assessed. A significant caveat is that increasing powder injection rate changes the conditions of the gas/particle flow interactions in the nozzle which can potentially alter the deposition characteristics. This is particularly true for processes where impact velocity of particles is slightly higher than the critical velocity (e.g., aluminum alloys sprayed with nitrogen) and in systems that operate at lower pressures. Cold spray systems with nozzles that operate at low pressures have a lower potential gas mass flow rate than a high pressure system that uses an identical nozzle regardless of geometry. Consequentially, the particle loading rate would be higher for the same powder feeding rate thus limiting the achievable deposition rate in comparison with a high pressure system. Several studies have been conducted to study powder feed rate effects on particle velocity and deposition quality (Ref 6, 7). Taylor et al. (Ref 7) have experimentally and numerically studied the effects of low powder feeding rates ranging between 1 g/min and 5 g/min. The authors (Ref 7) concluded that high quality coatings are possible with higher feeding rates if traverse robot speeds that move the nozzle are adjusted according to the feed rate. Meyer et al. (Ref 6) investigated the effects of particle shape and feeding rate on the velocity of particles exhausting from the exit of the nozzle using computational fluid dynamics (CFD) and particle image velocimetry (PIV). Their work showed losses in particle velocity with increasing powder feed rates and highlighted the importance of the powder feeding rate. Thus, it is important to understand the sensitivity and the limitations of the process to variations in particle loading rate, so that appropriate decisions can be made to optimize cost without sacrificing quality.

Optimization through advanced modeling of cold spray process parameters can be particularly useful for maximizing powder deposition rate while preventing adverse effects on the deposit. Prior studies have shown that, aerodynamically, the particle loading rate can be increased to much higher levels than traditionally used, with limited change to the particle impact velocities or temperatures (Ref 3, 8). Powder feeding rates across the industry are kept much below 5% of the gas mass flow rate (Ref 9, 10) to mainly prevent the gas flow from being affected by particles. Gilmore et al. (Ref 8) reported a particle velocity drop of only 6% as a result of increasing the particle loading rate from 1% to 10%. Recently, Ozdemir et al. (Ref 3) showed that much higher than traditionally accepted powder feeding rates can be implemented with minimal effects to the particle impact conditions.

An additional consideration that must be made for high powder feeding rate depositions involves the avoidance of local over-deposition and the preservation of coating quality (Ref 11, 12). Higher feeding rates without compensation on surface speed will result in significantly increased thickness per pass, which can affect the mechanical properties of the deposit (Ref 11, 12). Thin coating buildup layers have been shown to yield increased elastic modulus (Ref 12) and strength, and thus it is desirable to have many thin layers rather than a few thick layers. Increased powder deposition rates require high nozzle surface travel speeds reaching 2300 mm/s to maintain thin layering (roughly 60–200  $\mu\text{m}$ ) at very high deposition rates ( $> 100$  g/min). This poses a challenge for robotic nozzle manipulators (robotic arms, gantries, etc.) and may be a physical limitation for planar material deposition schemes. Such high travel speeds are difficult to achieve with industrial gantries and robots using planar raster schemes. Gantries and robots that are even capable of these speeds require large acceleration and deceleration zones (greater than 1 m) to reach their highest velocities. This is counter-productive as the practice would dramatically increase the time spent off the area of interest of deposition which wastes both gas and powder while decreasing deposition efficiency. Thus, achieving high rates of powder deposition can be limited by hardware especially when depositing material at high speeds on complex surfaces or small parts, where it may not be possible to maintain a very high nozzle surface velocity during the deposition. To address this difficulty, nozzle geometry can be designed to reduce gas flow rate while preserving the gas dynamics and holding the powder flow rate constant. This practice allows the adjustment of particle loading rate (powder to gas mass flow ratio) for the optimization of gas usage and planar deposition motion planning. Cylindrical components, on the other hand, can be placed on a lathe and spun at high speeds, which allows sufficiently high surface velocities for high rate deposition of cold spray coatings. Therefore, it is necessary to optimize the powder feeding rates, gas flow rates, deposition rates, and motion controls to optimize cost and achieve the desired deposition properties (Ref 3, 12). To do so, one must understand the consequences of these changes on the final product quality.

In this work, the effects of particle loading rate on mechanical properties of cold spray-deposited coatings are studied. Tantalum deposits were generated on hardened steel substrate specimens by varying particle loading rates from 5% to 14% of the process gas mass flow rate. Tantalum was selected due to its ease of processing by cold spray, its applications, and its properties. The material is of interest across many industries for a variety of components (e.g., furnace components, jet engine parts, electronics,

superalloy manufacturing) due to its density and refractory properties (Ref 13–15). Also, the density of tantalum allows its feeding rates to be easily adjusted to reach loading rates exceeding 15% utilizing powder feeders generally available with today's cold spray equipment.

The effects of increased loading rates on particle impact conditions were first studied from a fluid dynamic standpoint using validated computational fluid dynamics (CFD) models (Ref 3). The simulations showed minimal changes to particle impact conditions for particle loading rates up to 15%. The simulation outcomes were then tested with experiments to validate the prediction that much higher particle loading rates would not change the deposition quality. In four deposition scenarios, tantalum coating layering thicknesses (or buildup rates) on steel substrates were kept constant by increasing nozzle surface travel speeds in coordination with increasing powder deposition rates. Specimens were placed on a cylindrical fixture that was mounted on a lathe to achieve high nozzle surface travel velocities. Hardness of the coatings was tested using microhardness experiments. Relative measurements of bulk thermal properties of coatings were carried out to detect any potential differences in the bulk mechanical and microstructural properties of the coatings. Porosity was determined from the analysis of optical micrographs. Electron backscatter diffraction (EBSD) was used for microstructural comparison among the coatings.

## Computational Methods

### Two-Dimensional Computational Fluid Dynamics Simulations

A two-dimensional axially symmetric CFD model was implemented for simulating the gas flow in a commercial cold spray nozzle to estimate its effective expansion ratio using Siemens PLM Star-CCM + software (Plano, TX, USA). Continuity, momentum, and energy transport equations were used with the realizable shear-stress transport  $k-\omega$  turbulence model (realizable SST  $k-\omega$ ) (Ref 16–20). Temperature-dependent gas viscosity and thermal conductivity were chosen to more accurately capture the boundary layer development. Nozzle and substrate walls were assumed smooth with a nonslip boundary condition.

Polyhedral meshing techniques were applied along with near-wall mesh refinement to capture the boundary layer effects (Ref 21). Mesh refinement tests were conducted to verify that the solution is independent of the mesh size (Ref 18). The mesh resolution sufficiency was further analyzed by monitoring  $y^+$  values, which remained much below five on nozzle and substrate walls indicating a well-resolved boundary layer (Ref 21). Mach number calculated

throughout the nozzle yielded an effective nozzle expansion ratio to be used for one-dimensional CFD and experimental studies.

### Two-Way Coupled Quasi-One-Dimensional Computational Fluid Dynamics Simulations

The flow of helium (continuous phase) through the cold spray nozzle was calculated with the quasi-one-dimensional form of the governing equations of mass, momentum, and energy (Ref 18, 19, 22) as presented in Ozdemir et al. (Ref 3). Momentum and energy equations were two-way coupled with Lagrangian particles to account for force and thermal energy transfer between the gas and the particles. The validated and fully coupled quasi-one-dimensional model (Ref 3) was employed for its low computational cost and its effectiveness in estimating the influence of particle loading rates on the particle impact conditions. The effective area ratio of the nozzle found by two-dimensional models was applied in these one-dimensional models to account for boundary layer development.

Under the simulated conditions, volumetric flow ratio of the particles to the fluid remain well below 5% and the particle–particle nominal distances prove much higher than 10 particle diameters in the nozzle. Third-degree particle–particle interactions were therefore unlikely, and a two-way coupled model was found sufficient to handle the particle interactions (Ref 23). The equations were solved using the McCormack's predictor–corrector finite difference method (Ref 18, 22, 24) with a shock capturing scheme to handle high pressure gradients (Ref 18) that form due to the nozzle internal geometry. Methods detailed by Ozdemir et al. (Ref 3) were used to calculate the particle flow behavior. For simplicity, particles were assumed spherical, which was found sufficient to indicate the relative changes in the particle flight conditions due to the increased particle stream loading rates. Mass weighted averages of impact velocity, temperature, critical velocity, and the ratio of impact velocity to critical velocity were used to compare the relative changes in the particle impact conditions due to the particle loading effects. Mass averaged impact velocity is calculated by taking the dot product of the impact velocity vector  $(\overline{V}_{pi}(d_p))$  and the probability distribution function vector  $(\overline{PD}(d_p))$ .

## Experimental Methods

### Materials

Commercially available pure tantalum powder, Amperit 151.065 (H.C. Starck, Munich, Germany), was used for the

experiments. The received powder contains irregularly shaped particles with a mass weighted mean size of 23  $\mu\text{m}$ . The log-normal distribution variance was 0.39.

Substrates were made of 4140 steel with a typical hardness of HV 455. Two different size substrates were manufactured. Large samples were used for optical microscopy and EBSD. Small samples were used for hardness tests of the deposited surface. The large substrate dimensions were 76.2 mm by 25.4 mm by 12.7 mm in length, width, and thickness, respectively. The small substrate dimensions were 31.8 mm by 16.5 mm by 3.2 mm in length, width, and thickness, respectively.

### Cold Spray Process

Tantalum powder was deposited with a VRC Gen III Max cold spray system (Rapid City, SD, USA). A nozzle with an effective expansion ratio of 1.5 and a divergent section length of 77 mm was selected. The nozzle pressure and temperature were set at 5 MPa and 570°C, respectively. The nozzle standoff distance from the substrate specimens was kept constant at 20 mm during deposition for all samples. Expected deposition efficiency was calculated to be over 99% using the one-dimensional CFD models and methods outlined by Schmidt et al. (Ref 9, 25).

The specimens were mounted on a cylindrical fixture (Fig. 1) to achieve high surface travel velocities at high particle loading rates to keep the mass rate deposited per unit area per unit time identical between different test sets. After fastening, the substrate surfaces generated a radius of

approximately 50.5 mm in reference to the axis of the cylindrical fixture. The nozzle was directed perpendicular to the center of the substrates (90° spray incidence angle). Due to the planar surface of the substrates, however, a spray angle variation over the surface of the sample was unavoidable. The spray angle variation was between 74° and 104° for large specimens and was between 86° and 94° for small specimens. At the end of the sprays, a very minor spray thickness variation was observed with a slight height increase at the center of the large specimens. The peak coating thickness at the center of the large specimens was  $4.71 \pm 0.33$  mm and the minimum thickness at the edges of the coatings was  $4.51 \pm 0.36$  mm. Mean total coating thickness was 4.61 mm with a standard deviation of 0.34 mm as a result of deposition of 80 layers.

The nozzle traversed in the direction of the cylindrical fixture axis to deposit the powder material. The robotic motion and the lathe rotational speed were coordinated to increase nozzle-to-substrate surface travel speeds to keep the layer thickness and the number of layers identical for each particle loading rate. Table 1 summarizes the spray parameters that were used for each particle loading rate.

Substrate surfaces were cleaned by 600 grit SiC sandpaper. Immediately before the sprays, the surfaces were also cleaned by fine-grade Scotch-Brite™ pads and isopropyl alcohol.

### Powder Feed Rate Measurements

The VRC Gen III Max cold spray system utilizes a rotary drum powder feeder, and the powder feed rate is controlled by the rotational speed of a metering wheel. Theoretical volumetric output calculations allow the estimation of powder injection rate with the variation of the rotary wheel rotation speed. However, specific spray conditions and powder characteristics can result in minor deviations from the theoretical calculations. Differences in powder material, particle shape, and particle size distribution can alter the expected feeder output. Thus, powder feed rate measurements were done by weight measurements. The tantalum powder was weighed prior to filling the powder feeder. After each spray run, the amount of powder left in the powder feeder was weighed to determine the total amount of powder sprayed. The active spray time during a run was read from the logged data of the cold spray machine. Knowing the constant metering wheel speed, the actual powder feeding rate (g/min) was calculated and compared to the prediction. This allowed the calibrated calculation of particle loading rates throughout the tests.

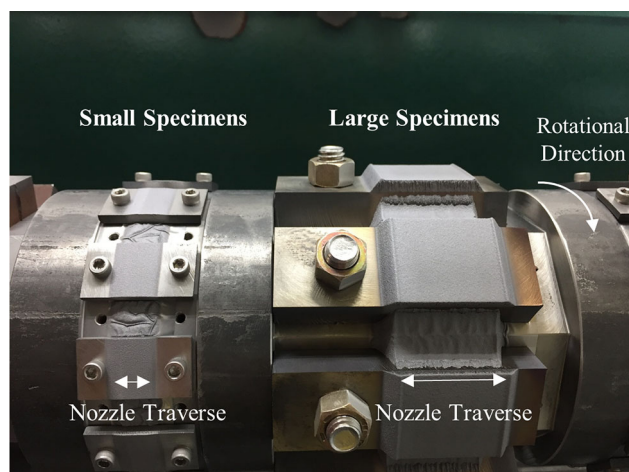


**Fig. 1** Image showing specimens after the spray procedure for test set #2. Twelve small and six large substrate specimens are mounted in a cylindrical manner to achieve high nozzle surface travel velocities by adjusting the cylindrical fixture rotational speed. Nozzle traverse speed is adjusted to keep layering thicknesses identical among the test sets. All small and large substrate specimens in each test set were produced simultaneously with identical spray parameters, surface conditions, and motion controls



**Table 1** Coordinated nozzle motion control parameters

Test set	Loading rate, %	Powder feeding rate, g/min	Surface travel speed, mm/s	Traverse speed, m/s
1	5	26.4	809	1.24
2	10	52.8	1612	2.49
3	12.5	66.0	2016	3.16
4	15	79.3	2420	3.73

## Hardness Tests

Hardness tests were performed with a Wilson Hardness Vickers 402 MVD microhardness tester (Lake Bluff, IL). Indentations were made on the polished top coating surfaces of three randomly selected specimens from each particle loading batch. A load of 4.903 N (500 g) was applied for indenting the samples. Several samples were initially tested by incrementally increasing loads to reduce local hardness variation effects. Indentation sizes generated by the 4.903 N force were on average 55  $\mu\text{m}$ , which is roughly twice the size of an average particle size. Ten indentations were produced on random surface locations per sample for a total of thirty hardness measurements for each batch.

## Porosity Measurements

Large specimens were cross-sectioned for porosity measurements. The metallographic sample preparation was conducted in accordance with ASTM E3 (Ref 26) using manual polishing. The porosity of the coating was measured using an Olympus Vanox-T AH-2 optical microscope (Tokyo, Japan) following the procedures detailed in ASTM E2109 (Ref 27). An open-source image analysis software, ImageJ (Ref 28), was used for porosity area percentage measurements. Prior to analysis, the samples were cleaned for 10 min in an ultrasonic cleaner while immersed in deionized water.

## Electron Backscatter Diffraction Characterization

Microstructural characterization was conducted with electron backscatter diffraction (EBSD). The metallographic samples used for porosity measurements were further polished with colloidal alumina (0.05  $\mu\text{m}$ ) for at least 14 h utilizing a Buehler Vibromet 2 vibratory polisher (Lake Bluff, IL). Pattern collection was performed using an Oxford Instruments HKLNordlys EBSD detector (Abingdon, United Kingdom) in a Zeiss Supra 40VP scanning electron microscope (Oberkochen, Germany) operating at an accelerating voltage of 20 kV. Scans were conducted at

1 kx and 2.5 kx magnifications with step sizes of 224 nm and 112 nm, respectively, using Oxford Instruments AZtec software. Hit rates ranged from 78% to 92%. Pattern quality and orientation maps were generated without noise reduction using Oxford Instruments HKL Tango software.

## Thermal Property Experiments

Differences in the bulk mechanical and microstructural characteristics of a homogenous material can be detected by thermal conductivity measurements (Ref 29–31). Characteristics such as porosity, grain structure, and particle-to-particle adhesion levels can affect the thermal conductivity of the deposited cold spray coatings (Ref 32). To detect any potential differences in the bulk tantalum microstructural properties due to increasing the particle loading and deposition rates, thermal property experiments were conducted. Three large specimens were prepared from each of the four particle loading rate experimental sets. Thermal property experiments were carried out using a Hot Disk 2500 S (Göteborg, Sweden) thermal property tester using the transient plane source (TPS) method, which allows for the measurement of thermal conductivity, thermal diffusivity, and specific heat. The TPS method uses a thin circular heating element that is sandwiched between two thin specimens of the same material. The resistance in the heating coils is also used to accurately measure the sensor average temperature. During the test, a constant power is applied across the heating element over a predetermined time period and the time transient change in the heating element average temperature is measured. The temperature curve is then used with built-in theoretical calculations (Ref 33) to accurately predict the thermal conductivity, thermal diffusivity, and the specific heat of the specimens. Due to the small size of the specimens, the thin strip (slab) version of the TPS method was implemented. In this method, outer boundaries of the specimens were insulated using polystyrene XPS foam. The most significant assumption in the experimental procedure is that the specimens are infinitely large in the planar direction (i.e., the specimen boundaries are far enough from the heating source so that the temperature pulse does not reach the

boundaries during the experiments). The thickness of the material is required to be between 31% and 80% of the radius of the heating element for the slab assumption. The method is insensitive to material shape or size beyond a temperature pulse penetration depth ( $\Delta_p$ ) in the planar direction when the samples comply with the thickness requirement. A Kapton 5465 F1 sensor with a radius of 3.2 mm was used. The sensor requires the slab samples to have a thickness of less than 2.52 mm. Sample dimensions and available probing depths are measured and listed in Table 2. The experimental time was adjusted to keep the heat wave penetration depth below the available penetration depth of the specimens.

The samples were first machined with a mill, and their measurement surfaces were hand finished using a 240 grit sandpaper. Sample thicknesses have a small deviation due to the wet sanding procedure, and all samples were kept well within the thickness required by the testing procedure (Ref 34). The thickness dimension of the cold spray coating samples is also the axis that is in-line with the spray direction. The experiments were conducted to test A, B, and C marked samples against each other by alternating the mating faces to be both substrate sides and both coating top sides. The experimental setup used for thermal property measurement is shown in Fig. 2. After appropriately fixturing the sensor and the specimens, the fixture was enclosed in a black box to isolate the specimens from the laboratory environment. This procedure was employed to avoid external effects such as radiation and/or air movement that may cause temperature gradients in the samples prior to the start of a given test.

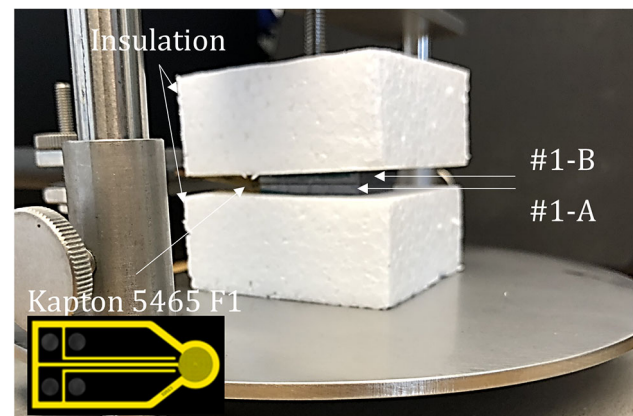


**Fig. 2** Image of the experimental setup prior to thermal property measurement shown with the representative image of a sensor

## Results

### Fluid Dynamic Effects of Particle Loading on Impact Conditions

Quasi-one-dimensional two-way coupled computational fluid dynamics simulations were first used to calculate the particle impact velocity ( $V_{pi}$ ) and temperature ( $T_{pi}$ ) by assuming negligible momentum and energy exchange between the fluid and the particles (i.e., ideal conditions). The results are shown in Fig. 3. This calculation provides a reference point from which relative changes to the particle impact conditions were determined. Ideal flow conditions yield a mass averaged particle impact velocity of 637 m/s and an impact temperature of 409 K. The critical velocity ( $V_{cr}$ ), under these conditions, was estimated with the semi-

**Table 2** Dimensions and available heat wave penetration depths of specimens

Particle loading rate, %	Sample ID	Thickness, mm	Width, mm	Length, mm	Available penetration depth, mm
5.0%	1-A	2.09	23.70	28.00	8.66
	1-B	2.00	24.68	29.43	9.15
	1-C	2.04	24.41	29.25	9.02
8.4%	2-A	2.06	24.21	29.38	8.92
	2-B	2.09	24.31	29.21	8.97
	2-C	2.06	24.34	29.30	8.98
10.3%	3-A	2.10	24.38	29.28	9.00
	3-B	2.09	24.26	29.26	8.94
	3-C	2.02	24.37	29.30	9.00
14.0%	4-A	2.08	24.39	29.34	9.01
	4-B	2.07	24.28	29.31	8.95
	4-C	2.06	24.35	29.31	8.99
Mean		2.06	24.31	29.20	8.96
Std. Dev.		0.03	0.22	0.38	0.11

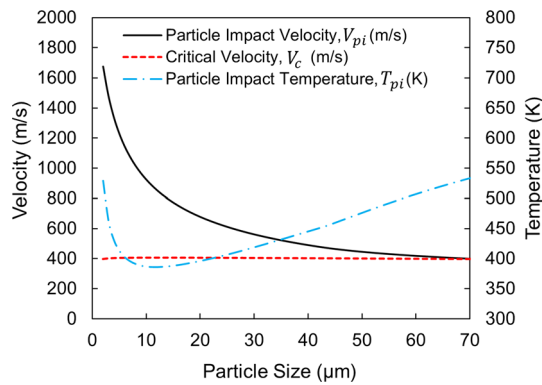


**Fig. 3** Tantalum particle impact conditions under ideal conditions, under which the gas-particle interactions are neglected

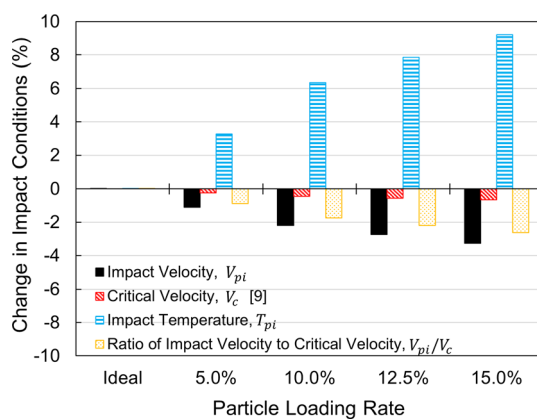


**Fig. 4** Mass averaged change in the impact velocity, impact temperature, and the ratio of impact velocity to critical velocity with respect to the ideal gas-particle flow conditions. Ideal flow conditions assume gas-particle interactions are negligible. Ideal conditions yield a mass averaged particle impact velocity of 637 m/s, impact temperature of 409 K, critical velocity of 406 m/s, and ratio of impact velocity to critical velocity of 1.57

empirical formulas developed by Schmidt et al. (Ref 9, 25). This estimation yielded a mass average  $V_{cr}$  of 406 m/s, above which particles are expected to adhere to the substrate and the previously deposited layers. Increases in  $V_{pi}$  beyond the  $V_{cr}$  (up to  $V_{pi}/V_{cr} = 2$ ) are expected to improve deposition efficiency and the overall coating properties. In general, when particles reach a velocity of greater than 150% of  $V_{cr}$ , deposits are found to provide good cohesive properties, low porosity, and good deposition efficiency as discussed by Schmidt et al. (Ref 25).

Changes in particle impact conditions with respect to the ideal gas-particle flow conditions are plotted in Fig. 4. The calculations show that the mass averaged particle impact velocity ( $V_{pi}$ ) decreases by no more than 3.5% at the highest particle loading rate and the mass averaged  $V_{pi}/V_{cr}$  ratio reduction was less than 3%. The aerodynamic effects

of higher particle loading rates are therefore expected to be minimal.

The magnitude of the changes in the particle impact velocity correlates strongly with the drop in  $V_{pi}/V_{cr}$ . A high percentage of increase in the particle impact temperature does not appear to be much of a factor. The drop in the momentum of the gas stream due to the increase in the particle loading rate is seen as a rise in the gas temperature. Particles, therefore, retain more of their initial thermal energy from the inlet of the nozzle to the exit of the nozzle while they travel through a higher temperature gas (Fig. 5).

Any increase in the impact temperature that is beneficial for aiding deposition is evidenced by a slight decrease in the critical velocity (Fig. 4), which is a function of the impact temperature (Ref 25). Additionally, the impact temperature effect due to particle loading rate is a strong function of particle size. However, the overall effect of changes in the particle impact temperature do not appear to be a strong factor in the magnitude of the changes in the ratio of the impact velocity to critical velocity ratio.

### Actual Powder Feeding Rates

Table 3 provides the powder feeding rates, loading rates, and deposition times for this study. Clearly there are minor differences between the actual powder feeding rates and the theoretically calculated powder feeding rates (Table 1). As previously noted, the powder output in relation to the rotary feeder wheel speed was measured prior to the experiments. The first two tests were Set 3 and 4. The feeder output was calibrated as the experiments progressed. Set 1 was the last experiment to be completed, and the powder feeder output matched the expected particle loading rate of 5%.

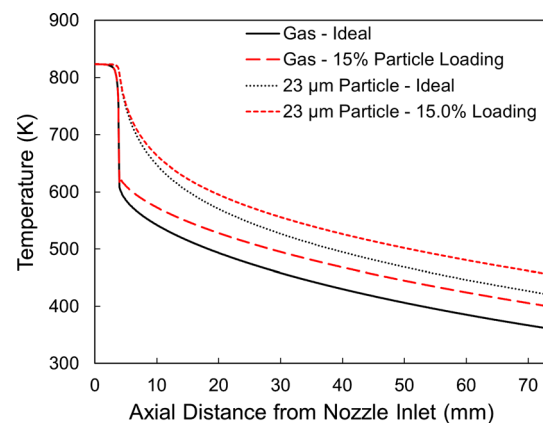


**Fig. 5** Gas and particle temperature from nozzle inlet to the nozzle exit under ideal and 15% particle loading conditions. Ideal case assumes gas-particle interactions are negligible. A 23  $\mu$ m particle represents the mass averaged particle size flow conditions

**Table 3** Actual powder feeding and loading rates determined by powder weight measurements

Test set	Test order	Actual powder feeding rate, g/min	Actual powder loading rate, %	Spray time, min
1	4	26.8	5.0	38.0
2	3	45.0	8.4	19.9
3	1	55.3	10.3	16.5
4	2	75.3	14.0	13.8

**Table 4** Mean microhardness values from the top coating surface of small specimens

Particle loading rate, %	5.0	8.4	10.3	14.0
Mean (HV)	313.0	306.7	298.5	298.1
Standard Deviation (HV)	13.1	12.8	13.6	14.6

### Hardness Tests Results

Hardness test results can be seen in Table 4. A statistical analysis of variance was performed on the data sets to quantify whether the average values from each particle loading set differ from each other. This test yielded that the means of the data sets are in fact different from each other. Although, the average hardness measured from the data sets show a slight drop as the particle loading rate increased with an overall decrease of 4.5% from a particle loading rate of 5% to 14%.

### Porosity Test Results

Porosity measurements were completed on the coatings of large samples. The results are listed in Table 5 from five images taken from each batch. The area percentage porosity in all samples remained below 1% with micrographs showing very low porosity in Fig. 6. No apparent trend was observed in relation to the particle loading rate (Table 5). While manual polishing procedures can have minor effects on porosity measurements (Ref 27), all of the samples had a similar appearance in micrographs.

### Electron Backscatter Diffraction Characterization

Figure 7 displays EBSD pattern quality maps for the coatings deposited with 5.0%, 8.4%, 10.3%, and 14.0% particle loading rates. In these maps, the grayscale intensity correlates with Kikuchi band contrast wherein black indicates poor diffraction pattern quality and white indicates

**Table 5** Porosity measurement results

Particle loading rate, %	5.0	8.4	14.0
Mean Porosity, %	0.57	0.09	0.24
Std. Deviation, %	0.27	0.04	0.06

high diffraction pattern quality. The coating deposition direction is oriented from top to bottom in each image.

The pattern quality maps reveal that all four coating microstructures are very similar to each other. The irregularly shaped tantalum powder particles appear highly deformed, and the absence of large areas of extremely low pattern quality indicates that porosity is low in the analyzed areas. The particle–particle interfacial regions exhibit lower pattern quality than the interior of the particles. This is typical of cold spray deposits where interparticle boundaries are characterized by refined grain structures and high dislocation densities. However, inspection of Fig. 7 also reveals that interparticle pattern quality is lower on average for the coating deposited at the 5.0% particle loading rate as particle boundaries are visibly darker relative to the interparticle regions in the other coatings. This observation indicates that the lower particle loading rate resulted in smaller grain sizes and higher defect densities in interparticle boundary regions, which correlates with the modeled changes in particle impact velocities and hardness measurements.

Figure 8 displays the Euler orientation maps that correspond to the pattern quality maps in Fig. 7. Zero solution pixels and grain boundaries with misorientation angles greater than 10° are black while the red, green, and blue levels in colored pixels are proportional to the three Euler angles. The orientation maps reveal that particle interiors consist of grains with sizes larger than 1  $\mu\text{m}$  while particle boundaries are characterized by the presence of ultra-fine grains (UFGs) with both elongated (“pancaked”) and equiaxed morphologies. Additionally, grains with high aspect ratios and lenticular shapes are observed throughout the scanned areas. Representative lenticular grains are identified by the white arrows in Fig. 8. These thin-lath



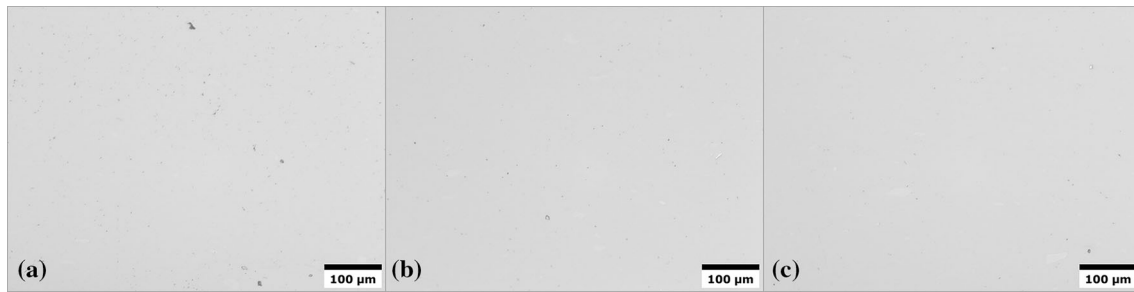


**Fig. 6** Cross-sectional micrographs from thick coatings samples sprayed at (a) 5% particle loading rate, (b) 8.4% particle loading rate, and (c) 14% particle loading rate. The spray direction was into the page

structures are likely deformation twins that formed due to the high rate of deformation during coating deposition. The presence of nonlinear twin segments and orientation gradients along twin lengths, shown in Fig. 9, indicates subsequent deformation occurred after twin nucleation during coating deposition. Significant twin activity has been reported in explosively driven high purity tantalum (Ref 35).

### Thermal Property Experiment Results

Thermal property experiments were conducted to detect any differences in the bulk deposition properties that may have occurred due to increased particle loading rates. The results of the experiments are listed in Table 6.

The overall average thermal conductivity in this work was measured to be 46.5 W/m·K, which is 15% lower than that of the reported thermal conductivity of wrought tantalum (54.4 W/m·K (Ref 36)). The overall thermal diffusivity and the specific heat of the tantalum coatings were measured as 21.9 mm<sup>2</sup>/s and 129.3 J/kg·K, respectively, with less than 10% difference in comparison with the values reported for wrought tantalum (Ref 36). The mean and the variance of the data sets of 5.0%, 8.4%, 10.2%, and 14% do not indicate a significant statistical difference.

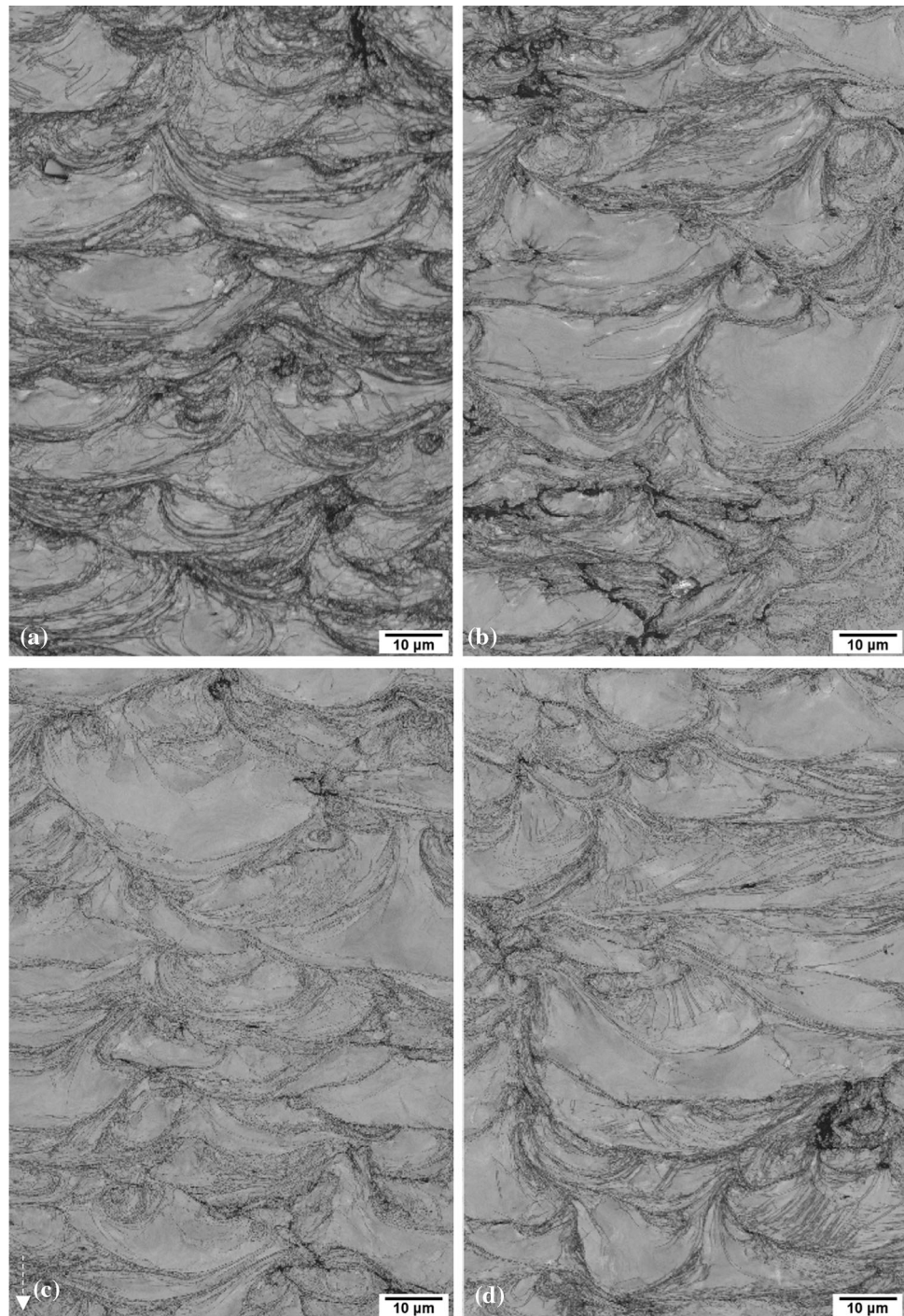
### Discussion

Computational fluid dynamics simulations and the experimental results both indicate that the particle loading rates can be increased to much higher than the generally adopted conservative range of less than 5%. CFD calculations showed that increasing the particle loading rate from 5% to 14% (9% increase) results in a drop of approximately 3.5% in the particle impact velocity in the case of tantalum sprayed in helium (Fig. 4). The results in this study are commensurate with the results reported by Gilmore et al. (Ref 8) for copper powder sprayed with air. Gilmore et al. (Ref 8) reported an impact velocity drop of 6% with an

increase in particle loading rate of 1% to 10% (9% increase). The drop in the particle impact velocity, indicated in this study by CFD calculations, is 1.5% lower than that reported by Gilmore et al. (Ref 8). Ozdemir et al. (Ref 3) showed that the spray conditions, the powder type, and the gas type can alter the trend in the particle impact velocity change due to particle loading rate. Therefore, the 1.5% difference in the particle impact velocity drop is justified for completely different spray conditions and gas-powder combinations.

Mechanical experiments (e.g., hardness tests) are great indicators of change in coating properties in parametric experiments of a given cold spray process (Ref 37, 38). Kumar et al. (Ref 38) showed that hardness tests yielded a clear trend when cold spray coating heat treatment conditions were systematically changed. In this study, an increase in the control parameter of particle loading rate from 5.0% to 14.0% yielded a minimal change of 4.5% in the hardness of the coatings. The porosity of the coatings in general was measured to be low and the results did not generate any discernible differences as the particle loading rate was increased with a maximum difference of 0.48%. The highest porosity value was measured as 0.57% for the 5% particle loading rate case while the lowest porosity was measured to be 0.09% for the 8.5% particle loading case. EBSD revealed that the microstructures of all four coatings were similar with only slight indications of variation in the interparticle boundary regions between the 5.0% particle loading rate case and the other conditions. The observed minor differences in grain structure and/or deformation levels can be correlated with differences in particle impact velocities wherein the higher impact velocities achieved at the lowest particles loading rate led to more severe plastic deformation at interparticle boundaries (Ref 39). The absence of extensive differences at the scale of the EBSD analysis supports the inferences made from mechanical property tests and porosity measurements that the quality of the depositions was not significantly altered by increasing the particle loading rate. This is further validated by the thermal property measurements. Sample sets

**Fig. 7** EBSD pattern quality maps for coatings deposited at (a) 5.0%, (b) 8.4%, (c) 10.3%, and (d) 14.0% particle loading rates. The spray direction for all specimens is indicated by the white dashed arrow in the lower left corner



produced with four different particle loading rates did not result in any significant differences in the thermal conductivity measurements. This indicates that the bulk structural characteristics of the tantalum coatings were not significantly altered by an increase in the particle loading rates between 5% and 14% (Ref 32).

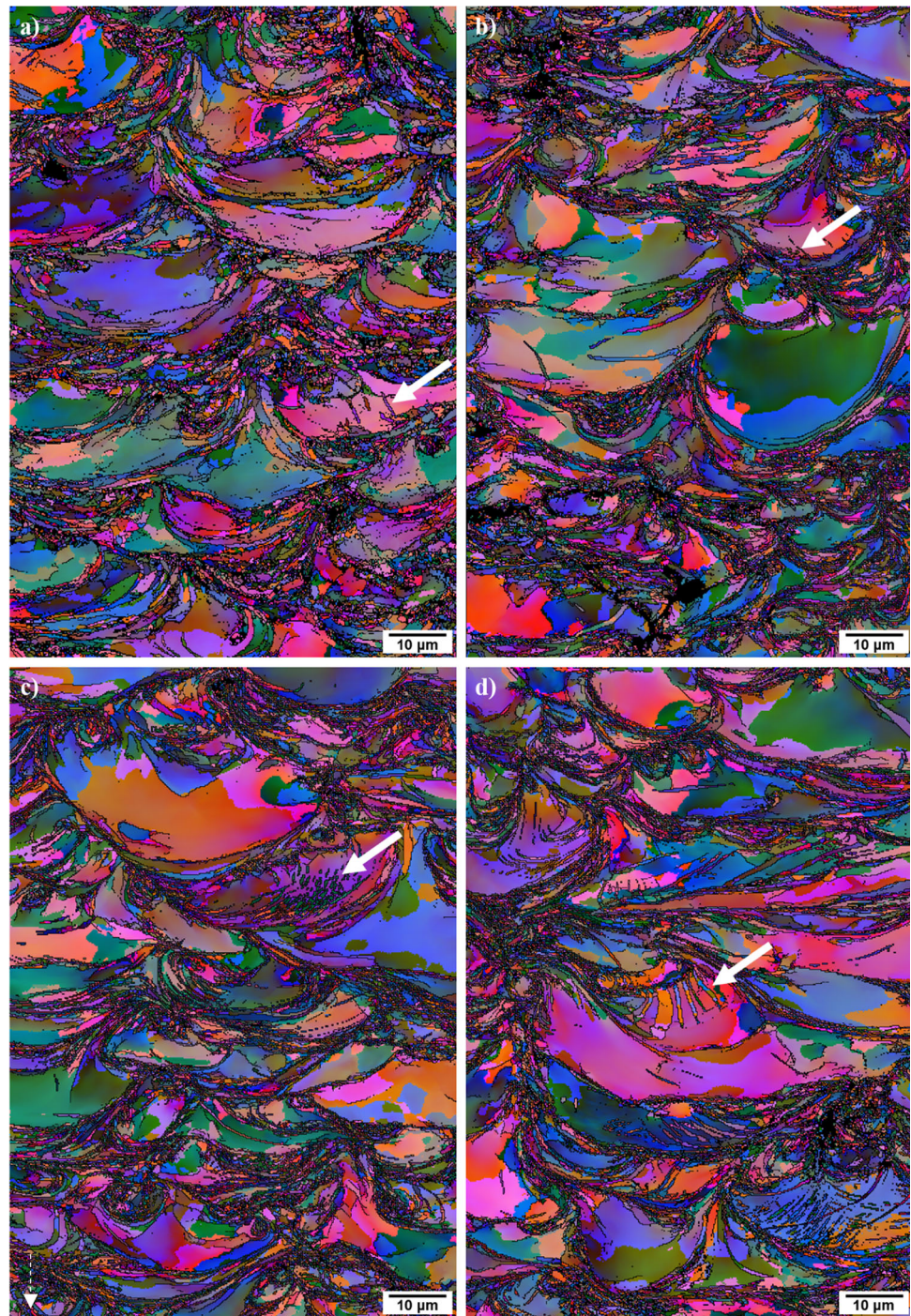
As a result of this work, the authors have demonstrated that much higher particle loading rates are possible with minimal effects to the particle impact conditions and to the

mechanical and the microstructural properties of the deposition. This is very promising for lowering the cost of cold spray processes in the future, as the gas can be used more efficiently to reduce its consumption rate per unit mass of deposited material.

In the case of processes that utilize helium, the biggest cost is associated with the gas when excluding labor and overhead costs. Helium can cost the private industry up to \$135/kg including transportation and storage depending on



**Fig. 8** EBSD Euler orientation maps for coatings deposited at (a) 5.0%, (b) 8.4%, (c) 10.3%, and (d) 14.0% particle loading rates. Black pixels indicate unindexed locations or high angle grain boundaries ( $> 10^\circ$ ). Arrows identify representative lenticular grains. The spray direction for all specimens is indicated by a white dashed arrow in the lower left corner



the geographical location of the facility. In today's cold spray systems, 2 mm nozzle throat diameters are common, and these systems can consume helium at 15 to 50 kg/h with costs roughly ranging between \$1900/h and \$6600/h depending on processing conditions. Although these costs seem high, it is possible to use helium recovery to theoretically recycle over 80% of the gas. Nevertheless, due to the higher properties and the lack of other options, cold spray with helium can still be the most cost-effective

solution for many high value repair, coating, and manufacturing applications (Ref 40, 41) with a high return on investment. The simplicity of the application once the optimal parameters have been developed allows the quick return of critical equipment back to service, equating to enhanced productivity in industrial settings. This study shows that the production rates can be increased even further with much higher powder deposition rates for cold spray manufacturing, as well as the effectiveness and the



**Fig. 9** EBSD Euler orientation maps depicting (a) possible nonlinear twin segments in the 10.3% particle loading rate sample (close up of Fig. 8c) and (b) possible twins with orientation gradients along their lengths in the 14.0% particle loading rate sample (close up of Fig. 8d). Black pixels indicate unindexed locations or high angle grain boundaries ( $> 10^\circ$ ). The spray direction is indicated by a white dashed arrow in the lower left corner

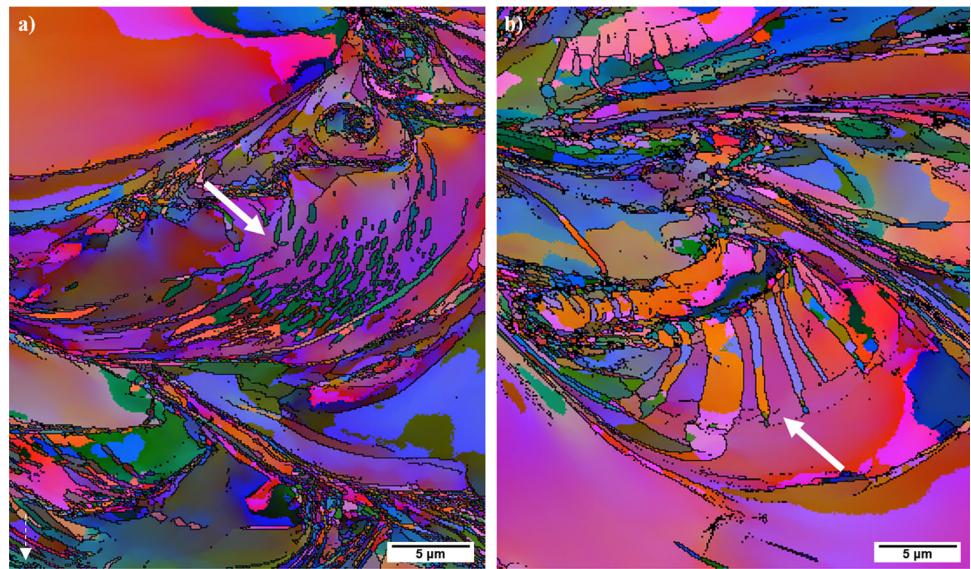


**Table 6** Experimental results from thermal property measurements at 21°C

Particle loading rate, %	Thermal conductivity, W/m-K		Thermal diffusivity, mm <sup>2</sup> /s		Specific heat capacity, J/kg K	
	Mean	SD	Mean	SD	Mean	SD
5.0%	46.1	0.7	22.0	3.3	128.9	22.2
8.4%	47.0	0.5	22.0	2.4	130.0	15.2
10.3%	46.8	1.1	21.5	2.2	132.1	13.1
14.0%	46.2	1.1	22.2	1.9	126.3	7.9
Overall	46.5	0.7	21.9	3.3	129.3	22.2
Wrought Tantalum (Ref 36)	54.4	...	23.6	...	139.0	...
Difference, %	14.5	...	7.0	...	7.0	...

efficiency of the cold spray process in general. High rate powder deposition helps with reducing labor costs by decreasing the time of deposition. Table 3 shows that the spray time for the same component was reduced from 38 min to 14 min when the powder deposition rate was increased from 27 to 75 g/min. Particularly for cylindrical components, where rotation speed can compensate for limitations in a robot's traverse speed, this method will help decrease overall process costs.

Caution must be taken when integrating higher than usual particle loading rates especially when using nitrogen or low pressure systems. As noted previously, the experiments presented in this study were conducted using helium with particle impact velocities that were approximately 1.6 times the critical velocity of tantalum. In applications where the base particle impact velocities are already only slightly above a material's critical velocity, an increase in the particle loading rate is expected to have a more pronounced effect on the deposition quality. For example,

aluminum alloy 6061 (Al6061) sprayed in nitrogen has a particularly low ratio of particle impact velocity to critical velocity (CVR) ( $\sim 1.2$  for a 30  $\mu\text{m}$  particle). Particle loading rates for Al6061 are also low, around 1%, due to the low density of aluminum. Under these conditions, an increase in particle loading rate from 1% to 5%, 10%, and 15% can lead to a CVR reduction of 6%, 12%, and 19%, respectively. The corresponding deposition efficiency values would be 100%, 99%, 80%, and 0% as predicted by models (Ref 3). In this case, smaller adjustments to the powder feeding rate would be more appropriate. Increasing the powder loading rate from 1% to 2% would still provide a 200% increase in deposition rate, while keeping the effects of particle loading rate on the resultant deposition quality relatively low. Thus, it is recommended to implement higher particle loading rates when: the particle impact velocity at low particle loading rates is considerably higher than the critical velocity; or when the loss in the deposition quality can be exchanged for process cost improvement.



A powder feeding rate increase is not the only way to increase particle loading rates. As mentioned previously, the particle loading rate is the ratio of powder feeding rate to the gas mass flow rate. The particle loading rate can also be increased by reducing the nozzle throat size to reduce gas flow rate while keeping the powder feeding rate constant. This adjustment would allow users to have a more cost-efficient application while keeping the powder deposition rates low for optimum layer thickness and mechanical properties. This strategy would be advantageous in planar powder deposition methods by keeping the required nozzle travel speeds low while implementing higher particle loading rates. In this way, the nozzle travel speeds would be more manageable by the industrial multi-axis robots and gantries.

## Conclusions

In this work, high powder feed rate deposition of tantalum was studied by producing coating specimens with varying ratios of the powder to helium mass flow rate ranging from 5% to 14%. The purpose of the analysis was to allow for more efficient use of the consumed gas in the cold spray process and to allow for efficiently increasing powder deposition rates in cold spray. The effects of the increase in tantalum particle concentration in the steady-state helium gas flow under process design conditions were studied via computational fluid dynamics simulations and experiments to demonstrate that increases in powder loading rates can be implemented with minimal or no impact on the particle impact velocities and temperatures.

The findings in this study demonstrate a method to save on the cost and production time of cold spray manufactured coatings, repairs, and components. The study also facilitates a more sustainable use of helium, which is effectively a nonrenewable resource.

**Acknowledgments** This work was sponsored in part by the U.S. Army Research Laboratories under the Grant Number W911NF-15-2-0026. Any opinions, findings, and conclusions or recommendations expressed in this material are those of the author(s) and do not necessarily reflect the views of the U.S. Government. The authors would like to thank Baillie Haddad and VRC Metal Systems for allowing the use of their microhardness equipment (Webster, MA, USA). The authors would also like to thank Lauren Randaccio and Joel Sanchez (Northeastern University, Boston, MA, USA) for assisting the cold spray experiments, Robert Allegretto (VRC Metal Systems, Rapid City, SD) in thermal conductivity sample preparation, and William Carpenter (South Dakota School of Mines and Technology, Rapid City, SD,) for EBSD sample preparation.

## References

1. K. Woock, Safeguarding our helium supply, *Imaging Economics*, 2013, p 8
2. The World Is Constantly Running Out Of Helium. Here's Why It Matters., (NPR) <https://www.npr.org/2019/11/01/775554343/the-world-is-constantly-running-out-of-helium-heres-why-it-matters>. (Accessed 18 February 2020)
3. O.C. Ozdemir, C.A. Widener, M.J. Carter, and K.W. Johnson, Predicting the Effects of Powder Feeding Rates on Particle Impact Conditions and Cold Spray Deposited Coatings, *J. Therm. Spray Technol.*, 2017, **26**(7), p 1598-1615
4. O. Stier, Fundamental Cost Analysis of Cold Spray, *J. Therm. Spray Technol.*, 2014, **23**(1), p 131-139
5. H. Gabel, Kinetic metallization compared with HVOF. (Tech Spotlight), *Adv. Mater. Processes*, 2004, **162**(5), p 47
6. M.C. Meyer, S. Yin, K.A. McDonnell, O. Stier, and R. Lupoi, Feed Rate Effect on Particulate Acceleration in Cold Spray Under Low Stagnation Pressure Conditions, *Surf. Coat. Technol.*, 2016, **304**, p 237-245
7. K. Taylor, B. Jodoin, J. Karov, Particle Loading Effect in Cold Spray, *J. Therm. Spray Technol.*, **15**(2), (2005)
8. D.L. Gilmore, R.C. Dykhuizen, R.A. Neiser, T.J. Roemer, and M.F. Smith, Particle Velocity and Deposition Efficiency in the Cold Spray Process, *J. Therm. Spray Technol.*, 1999, **8**(4), p 576-582
9. T. Schmidt, H. Assadi, F. Gartner, H. Richter, T. Stoltenhoff, H. Kreye, and T. Klassen, From Particle Acceleration to Impact and Bonding in Cold Spraying, *J. Therm. Spray Technol.*, 2009, **18**(5–6), p 794-808
10. V. Champagne, *The Cold Spray Materials Deposition Process: Fundamentals and Applications*, Woodhead Publishing Limited, Sawston, 2007, p 1-362
11. A. Moridi, S.M. Hassani-Gangaraj, S. Vezzu, and M. Guagliano, Number of Passes and Thickness Effect on Mechanical Characteristics of Cold Spray Coating, *Procedia Eng.*, 2014, **74**, p 449-459
12. S. Rech, A. Trentin, S. Vezzù, E. Vedelago, J.-G. Legoux, and E.J.J.O.T.S.T. Irissou, Different Cold Spray Deposition Strategies: Single- and Multi-layers to Repair Aluminium Alloy Components, *J Thermal Spray Technol*, 2014, **23**(8), p 1237-1250
13. S.M. Cardonne, P. Kumar, C.A. Michaluk, and H.D. Schwartz, Tantalum and Its Alloys, *Int. J. Refract. Met. Hard Mater.*, 1995, **14**, p 187-194
14. J. Kim, G. Bae, and C. Lee, Characteristics of Kinetic Sprayed Ta in Terms of the Deposition Behavior, Microstructural Evolution and Mechanical Properties: Effect of Strain-Ratedependent Response of Ta at High Temperature, *Mater. Charact.*, 2018, **141**, p 49-58
15. M.D. Trexler, R. Carter, W.S. De Rosset, D. Gray, D. Helfritsch, and V.K. Champagne, Cold Spray Fabrication of Refractory Materials for Gun Barrel Liner Applications, *Mater. Manuf. Processes*, 2012, **27**, p 820-824
16. Spotlight on Turbulence: STAR-CCM + v11.06, (Siemens PLM Software) [https://steve.cd-adapco.com/articles/en\\_US/FAQ/Spotlight-on-Turbulence](https://steve.cd-adapco.com/articles/en_US/FAQ/Spotlight-on-Turbulence)
17. STAR-CCM + Release Notes v11.06, (Siemens PLM Software) <https://steve.cd-adapco.com/>. (Accessed 4 Jul 2017)
18. J.D.J. Anderson, *Computational Fluid Dynamics: The Basics with Applications*, McGraw-Hill Inc., New York, 1995, p 1-547
19. R.B. Bird, W.E. Stewart, E.N. Lightfoot, *Transport Phenomena*, 2 ed., John Wiley and Sons, Inc, 2002, p 27, 276, 439
20. F.R. Menter, Review of the Shear Stress Transport Turbulence Model Experience from an Industrial Perspective, *Int. J. Comput. Fluid Dyn.*, 2009, **23**(4), p 305-316

21. H. Schlichting, *Boundary Layer Theory*, 7 ed., F.J. Cerra, Ed., McGraw-Hill Book Company, Inc, 1987, p 596–667
22. J.F. Wendt, *Computational Fluid Dynamics: An Introduction*, 3rd ed., Springer, Berlin, 2009
23. S. Martin and J.R. Williams, *Multiphase Flow Research*, Nova Science Publishers Inc., New York, 2009
24. J.D. Anderson, *Modern Compressible Flow with Historical Perspective*, McGraw-Hill Inc., New York, 2012
25. T. Schmidt, F. Gartner, H. Assadi, and H. Kreye, Development of a Generalized Parameter Window for Cold Spray Deposition, *Acta Mater.*, 2006, **54**, p 729–742
26. ASTM, Standard Guide for Preparation of Metallographic Specimens, ASTM E3, ASTM International 2017
27. ASTM, Standard Methods for Determining Area Percentage Porosity in Thermally Sprayed Coatings, ASTM E2109 - 01, ASTM International 2014
28. ImageJ, <https://imagej.net/ImageJ>. (Accessed 7 Jan 2019 2019)
29. B. Li, L. Hou, R. Wu, J. Zhang, X. Li, M. Zhang, A. Dong, and B. Sun, Microstructure and Thermal Conductivity of Mg-2Zn-Zr Alloy, *J. Alloys Compd.*, 2017, **722**, p 772–777
30. E. Vandersluis, A. Lombardi, C. Ravindran, A. Bois-Brochu, F. Chiesa, and R. MacKay, Factors Influencing Thermal Conductivity and Mechanical Properties in 319 Al Alloy Cylinder Heads, *Mater. Sci. Eng. A*, 2015, **648**, p 401
31. C. Yang, F. Pan, X. Chen, N. Luo, B. Han, and T. Zhou, Thermal Conductivity and Mechanical Properties of Sm-Containing Mg-Zn-Zr Alloys, *Mater. Sci. Technol.*, 2018, **34**(2), p 138–144
32. D. Seo, K. Ogawa, K. Sakaguchi, N. Miyamoto, and Y. Tsuzuki, Parameter Study Influencing Thermal Conductivity of Annealed Pure Copper Coatings Deposited by Selective Cold Spray Processes, *Surf. Coat. Technol.*, 2012, **206**(8–9), p 2316–2324
33. S.E. Gustafsson, Transient Plane Source Techniques for Thermal Conductivity and Thermal Diffusivity Measurements of Solid Materials, *Rev. Sci. Instrum.*, 1991, **62**(3), p 797–804
34. Hot Disk Thermal Constants Analyser Instruction Manual, *Hot Disk*, Göteborg, Sweden, 2019
35. V. Livescu, J.F. Bingert, and T.A. Mason, Deformation Twinning in Explosively-Driven Tantalum, *Mater. Sci. Eng. A*, 2012, **556**, p 155–163
36. ASM Handbook Volume 02 - Properties and Selection: Nonferrous Alloys and Special-Purpose Materials, ed., ASM International, 1990
37. G. Bolelli, B. Bonferroni, H. Koivuluoto, L. Lusvarghi, and P. Vuoristo, Depth-Sensing Indentation for Assessing the Mechanical Properties of Cold-Sprayed Ta, *Surf. Coat. Technol.*, 2010, **205**(7), p 2209–2217
38. S. Kumar, V. Vidyasagar, A. Jyothirmayi, and S. Joshi, Effect of Heat Treatment on Mechanical Properties and Corrosion Performance of Cold-Sprayed Tantalum Coatings, *J. Therm. Spray Technol.*, 2016, **25**(4), p 745–756
39. M.R. Rokni, S.R. Nutt, C.A. Widener, V.K. Champagne, R.H. Hrabe, Review of Relationship Between Particle Deformation, Coating Microstructure, and Properties in High-Pressure Cold Spray, *J. Therm. Spray Technol.*, (2017)
40. C.A. Widener, M.J. Carter, O.C. Ozdemir, R.H. Hrabe, B. Hoi-land, T.E. Stamey, V.K. Champagne, and T.J. Eden, Application of High-Pressure Cold Spray for an Internal Bore Repair of a Navy Valve Actuator, *J. Therm. Spray Technol.*, 2016, **25**(1–2), p 193–201
41. B.L. James, B-1 Cold Spray Initiative, Cold Spray Action Team Meeting, (Worcester, MA, USA, 2016)

**Publisher's Note** Springer Nature remains neutral with regard to jurisdictional claims in published maps and institutional affiliations.